Crystal structure, DFT, molecular docking and dynamics simulation studies of 4,4-dimethoxychalcone

M.V. Yashwanth Gowda[a], B.L. Vinay[a], N. Maitra[a], S.R. Kumaraswamy[b] and N.K. Lokanath[a*]

[a]*Department of Studies in Physics, University of Mysore, Manasagangotri, Mysuru 570 006, India*
[b]*Department of Physics, Maharani's Science College for Women, Mysuru 570 0 05, India*

CHRONICLE	ABSTRACT
	In the current study, the compound 4,4-dimethoxychalcone (DMC) was structurally studied and analyzed by *in silico* approach against M^{pro} to investigate its inhibitory potential. The molecular structure of the compound was confirmed by the single crystal X-ray diffraction studies. The crystal structure packing is characterized by various hydrogen bonds, C-H…π and π…π stacking. Intermolecular interactions are quantified by Hirshfeld surface analysis and the electronic structure was optimized by DFT calculations; results are in agreement with the experimental studies. Further, DMC was virtually screened against SARS-CoV-2 main protease (PDB-ID: 6LU7) using molecular docking, and molecular dynamics (MD) simulations to identify its inhibitory potential. A significant binding affinity exists between DMC and M^{pro} with a -6.00 kcal/mol binding energy. A MD simulation of 30ns was carried out; the results predict DMC possessing strong binding affinity and hydrogen-bonding interactions within the active site during the simulation period. Therefore, based on the results of the current investigation, it can be inferred that a DMC molecule may be able to inhibit M^{pro} of COVID-19.

1. Introduction

An exceptional class of naturally occurring chemicals can be categorized as flavonoids with a 1,3-diarylpropane skeleton. The open-chain unsaturated carbonyl system is known as chalcones or 1,3-diphenyl-2-propen-1-one derivatives which consists of two aromatic rings linked by three carbons. They are commonly found in citrus fruit, vegetables and spices. Chalcones are a class of yellow pigments termed as anthochlor pigments. As secondary metabolites of terrestrial plants, chalcones are thought to be the progenitors of flavonoids and isoflavonoids and have a variety of biological actions. Chalcones are common intermediates used to create a variety of heterocyclic compounds,[1] including flavones, isoxazoles, pyrazoles, and tetrahydro-2chromens.[2] Natural or artificial chalcones have a variety of biological functions that are known in addition to pioneering work in the synthesis of naturally occurring chemicals Kostanecki[3] was the first to coin the name chalcone. The most commonly used chemical synthesis method is the Claisen–Schmidt condensation of the corresponding aromatic aldehyde and 2 hydroxyacetophenones in alkaline or acid catalysis[4]. Numerous biological activities and therapeutic activities of the chalcones have been reported which includes inhibition of chemical mediator release, inhibition of leukotriene B4, inhibition of tyrosinases, and inhibition of aldose 4 reductase as well as anti-cancer,[5] anti-leishmanial,[6] anti-fibrogenic[7], anti-inflammatory,[8] immunomodulatory,[9] anti-platelet,[10] anti-ulcerative, antiviral, antioxidant, antitubercular, and anti-hyperglycemic. The biological activities of chalcones are determined by the presence of a reactive, alpha and beta unsaturated keto function.[11]

Multi-drug resistance microbial infections have rapidly increased in occurrence over the past few decades, and this has caused serious health care issues. Therefore, finding new antimicrobial drugs will always be a crucial and difficult challenge for medicinal chemists. On March 12, 2020, the World Health Organization reported the Covid-19 an emerging disease, in order to treat infected people globally, studies on the COVID-19 virus are being conducted by a number of scientific communities.[12-16] The main protease of corona virus (M[pro]) splits the polyproteins into individual fragments, which promotes the growth of new viruses.[7-19] The main protease is the best-characterized target for SARS-CoV-2 because it facilitates viral multiplication and transcription, and multiple groups have described the crystal structure of the main protease with and without the inhibitor.[20-23] Finding effective M[pro] inhibitors can stop the COVID-19 virus from replicating in the host cell. Therefore, inhibiting the activity of this enzyme would prevent viral transcription and replication, which would aid in the development of novel medications.[24] In this study, our effort is to examine the potential of 4,4-Dimethoxychalconecompound as an M[pro] inhibitor. We used *in silico* approach (molecular docking and dynamic simulation) to analyse the binding mode and dynamic properties of ligand and protein. The current research work includes structural elucidation with X-ray diffraction method, Hirshfeld surface and energy framework analysis, density functional theory calculations, molecular docking and dynamic simulation studies.

2. Results and discussion

2.1 Crystal structure analysis

Single crystal X-ray structural analysis confirmed that the DMC molecule is crystallized in a orthorhombic $P2_12_12_1$ space group with four independent molecules in its unit cell (Z=4). The ORTEP diagram with atom numbering scheme is depicted in (**Fig. 1a**). The crystal structure and refinement parameter of the DMC molecule are summarized in (**Table 1**). Structural analysis of DMC molecules is revealed that the methoxy group distorts the planarity of the molecular structure by deviating O1 about 0.142 Å from the plane of benzene ring (**Fig. 1b**). Various intra and intermolecular hydrogen bond interactions, C-H....*Cg*, *Cg*...*Cg* and inter molecular short interactions played a crucial role in stabilizing the crystal structure of DMC. The C10-H1...O2 intra molecular hydrogen bond interaction form a five member ring [S(5): graph-set notation] with the bond length 2.459 Å shown in the figure 1c. The C17-H17...O2 involved in strong intermolecular hydrogen bond interaction with a donor acceptor distance of 2.661 Å, directing DMC molecules to arrange adjacently in zig-zag manner along b-axis (**Fig. 2c**). Despite C-H...O intermolecular hydrogen bond interactions, C-H...Cg [C3-H3...Cg1: H3-Cg1; 2.96 Å, C3-Cg1; 3.730° Å, C3-H3...Cg1; 141.00° and symmetry code: -1/2+x, 3/2-y, -z] intermolecular contact exceedingly contributes to the crystal structure stability of DMC (**Fig. 2a and Table 2**). Intermolecular *Cg*...*Cg* interactions between the centroids of methoxy rings [Cg1-Cg1: 4.938(6) Å] and adjacent methoxy rings [Cg1-Cg2: 5.193(5) Å] are also contributed in the crystal packing of DMC (**Fig. 2b and Table 2**).

Table. 1. Crystal data and structure refinement details of DMC.

|	
Empirical formula	$C_{17}H_{16}O_3$
Formula weight	268.30
Temperature	293 K
Wavelength	1.54178 Å
Crystal system	Orthorhombic
Space group	$P2_12_12_1$
Cell dimensions	$a = 5.2847(18)$Å
	$b = 8.674(4)$Å
	$c = 30.681(11)$Å
	$\alpha = 90°$
Volume	1406.4(10) Å³
Z	4
Density(calculated)	1.267 Mg m⁻³
Absorption coefficient	0.697 mm⁻¹
$F000$	568
θ range for data collection	2.88° to 65.04°
Index ranges	$-5 \leq h \leq 6$
	$-9 \leq k \leq 10$
	$-35 \leq l \leq 35$
Reflections collected	6046
Independent reflections	2218 [$R_{int} = 0.0748$]
Refinement method	Full matrix least-squares on F^2
Data / restraints / parameters	2218 / 0 / 183
Goodness-of-fit on $F2$	1.014
Final [$I > 2\sigma(I)$]	$R1 = 0.0952$, $wR2 = 0.2565$
R indices (all data)	$R1 = 0.2023$, $wR2 = 0.3610$
Extinction coefficient	CIF-file generated for gkn8 R = 0.10
Largest diff. peak and hole	0.259 and -0.339 e/Å⁻³
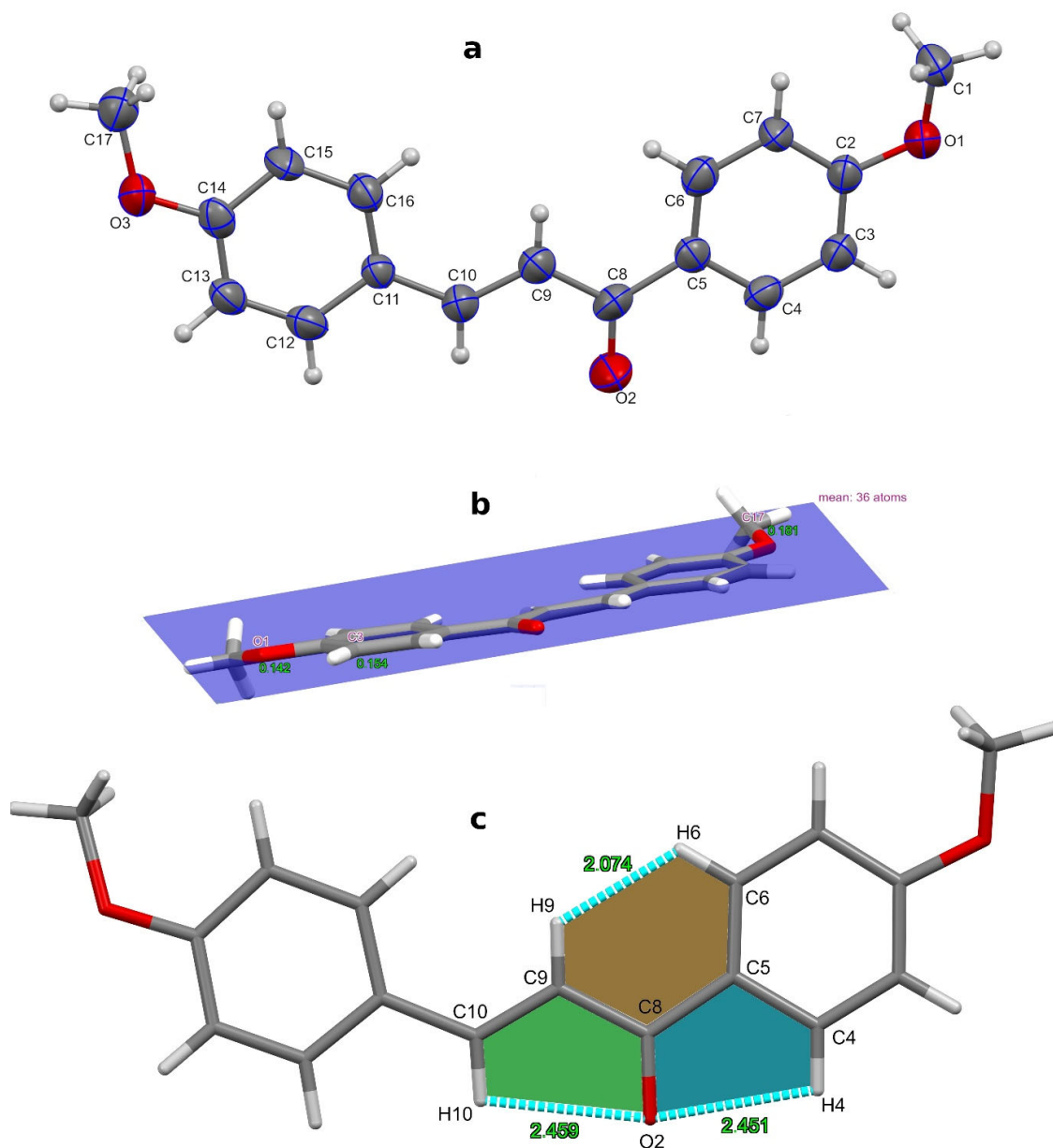
Fig. 1. (a) *ORTEP* with atom numbering scheme where thermal ellipsoid are drawn at 50% probability, (b) planarity representation and (c) Supramolecular S(5) ring motif due to C10-H1...O2 intramolecular hydrogen bond interaction in DMC molecule.

Table. 2. X-H… Cg [X=C] and Cg-Cg interactions of title compound.

X…H	Cg(J)	H...Cg (Å)	H (Å)	γ (°)	X-H...Cg (°)	X...Cg (Å)	X-H...Cg (°)
C3-H3	Cg(1)[i]	2.96	2.88	13.37	141.00	3.730(10)	51

X=C; i(symmetry)=-1/2+x,3/2-y,-z ; Cg(1): C2-C3-C4-C5-C6-C7

Short Ring-Interactions

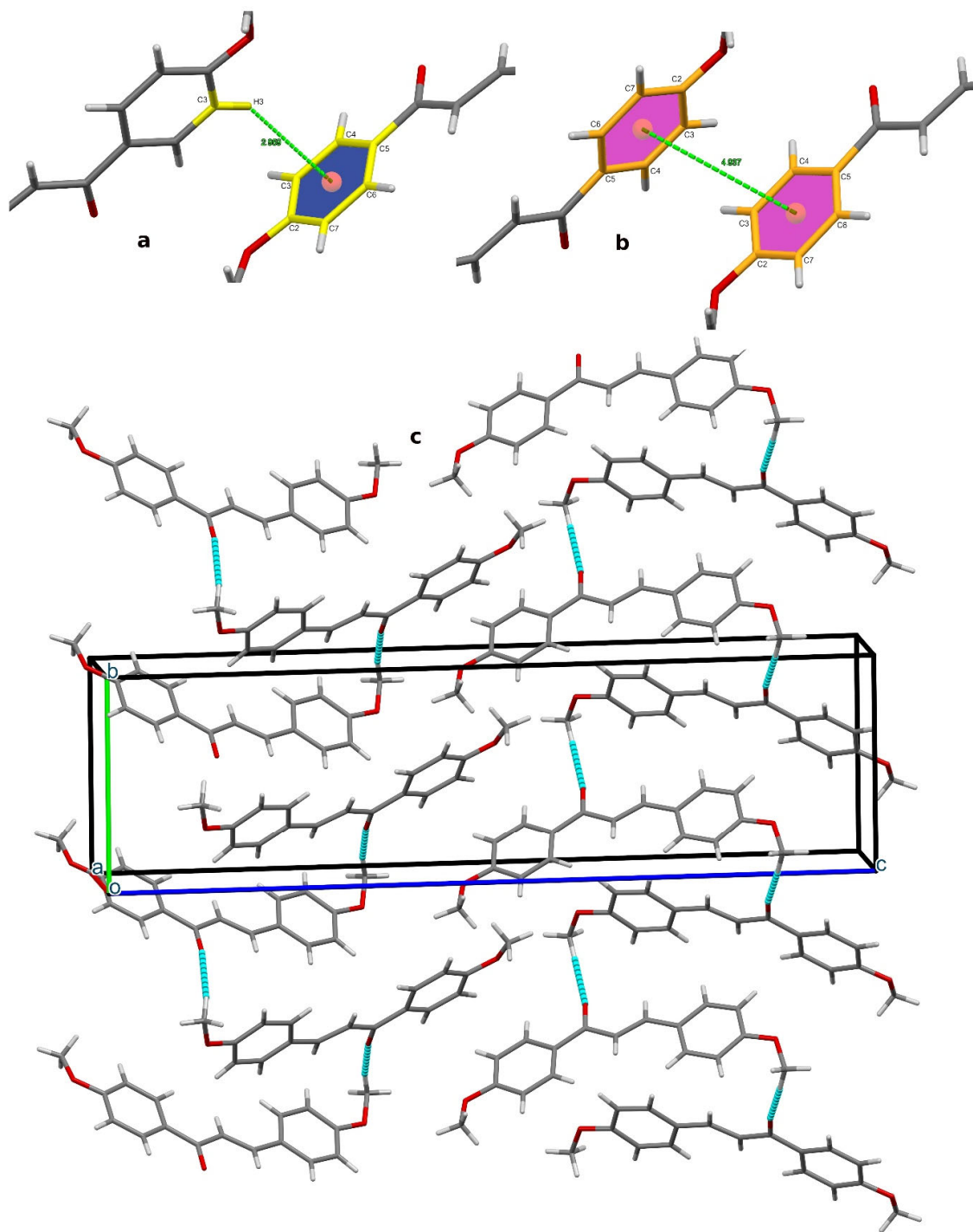| Cg(I)	Cg(J)	Cg-Cg	α	β	γ	Cg(I)⊥	Cg(J)⊥	Symmetry code
Cg(1)	Cg(1)	4.938(6)	72	19.5	71.6	1.559(4)	4.653(4)	*1/2+x,3/2-y,z*

Cg(1): C2-C3-C4-C5-C6-C7

Fig. 2. (a) Intermolecular C-H...Cg and (b) Cg...Cg interactions between the adjacent molecules and (c) molecular packing diagram along *a*-axis where, blue colored dotted lines indicates the intermolecular C-H...O hydrogen bond interactions.

2.2 Hirshfeld surface analysis

Various non-covalent interactions contribute to the architecture of DMC molecules. The non-covalent interactions in the lattice space are visualized via 3D electron density map. HS analysis is an effective tool to explore the nature of packing and contribution of intermolecular interactions present in the compound can be achieved by analysis of the Hirshfeld surface. HS plotted over a normalized contact distance d_{norm} ranging from -0.040 to 1.249 a.u. Shape index with a transparent view ranging from -0.360 to 0.909 a.u and curvedness with a transparent view in the range from -1.375 to 0.370 visualized in (**Fig. 3b and Fig. 3c**). The d_{norm} surface for the DMC (**Fig. 3a**) suggests the existence of intermolecular hydrogen bond interactions, in which a total six red spots appeared on surfaces suggest the existence of intermolecular hydrogen bond contacts. The deep red spot on HS shown in the figure indicates the C-H...O hydrogen bond interactions in the crystal, which is responsible for zig-zag molecular chains along the b-axis. In the (**Fig. 3b**), it is observed that triangle shaped red patches on the shape index surface also interact with large flat regions across the molecule visible on the curved surfaces evidence the C-H...*Cg* and *Cg-Cg* interactions. The molecule shows red (hydrogen bond acceptors) colored regions around the oxygen atom (O1, O2, and O3), indicating the electronegative spot.

2D fingerprints (FPs) plots, relative percentage and its graphical representations are shown in the figure 4. The characteristic spike at $d_e + d_i$ 2.3 A resembles the shortest H-H contact and the precise feature of the FPs shows the distinct splitting of the short H-H fingerprint in the DMC molecule. The broad region with short and narrow spikes in the middle of the plot is associated as a major contributor to the crystal packing. H-H interactions comprising 42% of the overall interactions are dominant among the total interactions responsible for crystal packing. The C-H short interactions comprising 36% are the second key contributor to the crystal packing. The C-H...O contacts appear as a pair of characteristic tips in the fingerprint plots comprising 21.3% on the total Hirshfeld surface are C17-H17C...O2 and C1-H1B...O3 with a bond length 2.551 and 2.512 Å respectively (**Fig. 4**). The blue-green region on the FPS represents the *Cg*...*Cg* interactions also play a vital role in stabilizing the molecular packing.
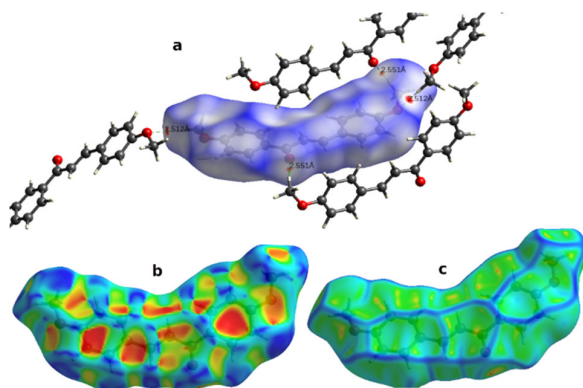

Fig. 3. Hirshfeld surface (a) mapped with d_{norm} and neighbouring molecules along with distance (b) shape index surface and (c) curvedness of DMC molecule
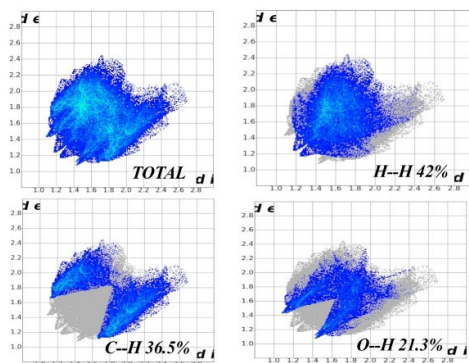

Fig. 4. 2D fingerprints and relative percentage (%) contributions to the total HS from various interactions.

2.3 Energy frame work analysis

Energy framework analysis is a precise and unique technique, performed using CrystalExplorer 17.5 software with the aid of crystallographic information file for visualizing the supramolecular architecture based on pairwise interaction energies. This analysis helps us to understand the nature of interaction energies between the pairs of molecules via 3D graphical representation. Within the radius of 3.8 Å interaction energies are evaluated and visualized through the energy framework. Relative strengths and types of the interactions in various directions can be represented by cylinders with the help of colour coding. Cylinder radii are proportional to the strength of the interactions. Selected clusters of molecules, interactions, energies and results are shown in the (**Fig. 5**). Cluster of molecules with cylinders colours corresponds to various types of energy profiles electrostatic (E_{ele}), dispersion (E_{disp}), polarization (E_{pol}), and repulsion (E_{rep}) energies sum of these energies resulting in total energy. In a cluster of molecules, yellow and green coloured molecules at a distance 10.68 and 6.89 Å connected to the centroid having interaction energies -17.3 kJ/mol and -26 kJ/mol respectively. Calculated total interaction energies of the DMC molecule are electrostatic (E_{ele} = -38.8976 kJ/mol), polarization (E_{pol} = -8.806 kJ/mol), dispersion (E_{disp} =-135.528 kJ/mol), repulsion (E_{rep} = 53.6424 kJ/mol) summing of these energies provides the total energy (E_{tot} = -129.589kJ/mol) with scale factor 1.057, 0.74, 0.871 and 0.618 respectively. The energy framework analysis confirms the dominance of the dispersive energy over the electrostatic, polarisation and repulsive energies.
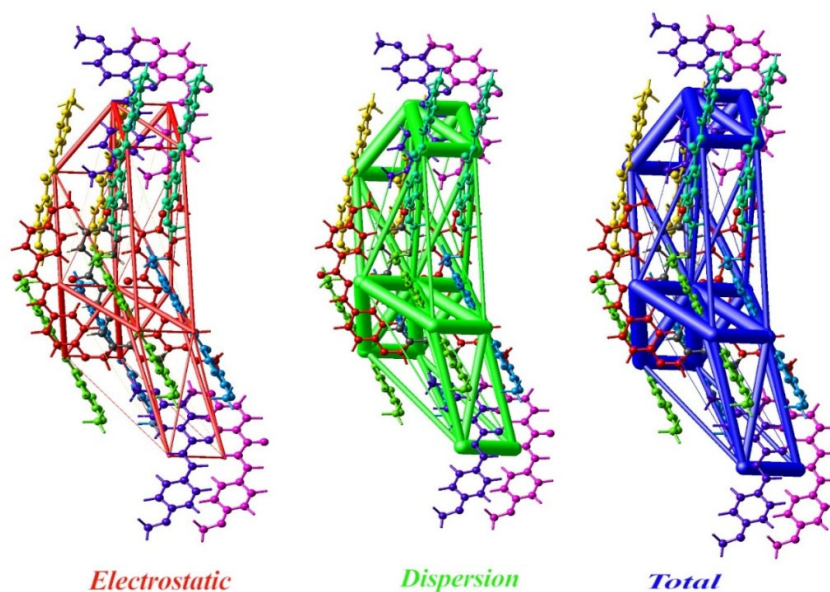
Fig. 5. Packing modes of molecules and energy framework diagrams for electrostatic (E_{ele}), dispersion (E_{disp}) and total energy (E_{tot}) for cluster of nearest neighbour molecules in DMC molecule.

Table. 3. Molecular interaction energies of DMC, (N) refers to number of molecules with R(A) molecular centroid to centroid distance and energies are in kJ/mol.

	N	Symop	R	E_ele	E_pol	E_dis	E_rep	E_tot
	2	x, y, z	5.28	-4.5	-2.5	-38.9	17.3	-29.8
	2	x+1/2, -y+1/2, -z	10.68	-4.6	-1.1	-21.5	11.4	-17.3
	2	-x, y+1/2, -z+1/2	6.89	-8.1	-3.7	-30.3	18.9	-26
	2	x+1/2, -y+1/2, -z	12.86	-1.7	-0.9	-14.9	8.6	-10.1
	2	-x, y+1/2, -z+1/2	7.58	-10.9	-2.2	-35.5	19.1	-32.2
	2	-x+1/2, -y, z+1/2	15.65	-7.6	-1.1	-10.1	8.4	-12.5
	2	-x+1/2, -y, z+1/2	16.82	0.6	-0.4	-4.4	3.1	-1.6

2.4 DFT calculations

The electronic structure of the DMC molecule was further analysed by quantum computational (DFT) studies. The ground state optimization of the molecule in the singlet spin state energy of the system with the minima point is found to be -833.3233 Hartree in order to get most possible electronic structure conformation which is performed using B3LYP calculation method with 6-311+G(d, p) basis set. The geometrical parameters such as bond lengths, bond angles and tensional angles (DFT and XRD) are depicted in supplementary (**Table S1 and S2**). The optimized geometrical parameters are well in agreement with the crystal structure data. However, the theoretical calculations have been carried out in the gas phase and experimental parts performed in the solid phase. By comparing these data, shows that the theoretical values are slightly greater than the experimental results. Superposition the molecular structure obtained by XRD and DFT analysis is shown in the (**Fig. 6**). The root mean square deviation is found to be 0.4 Å.
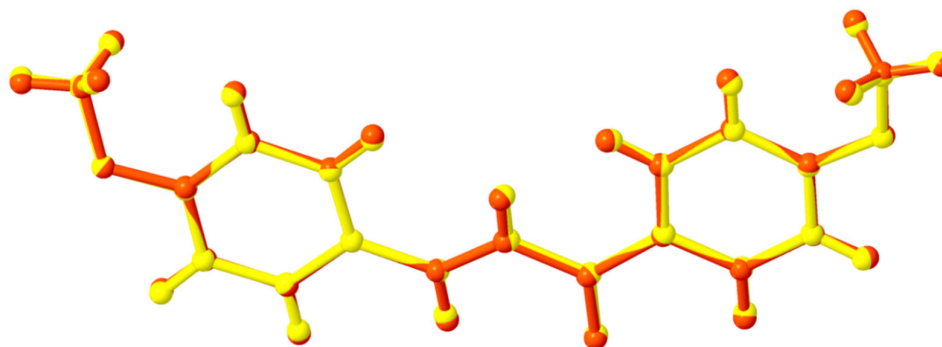

Fig. 6. Overlay of the X-ray crystal structure and optimized electronic structure of DMC molecule.

2.5 QTAIM and NCI analysis

In accordance with Bader's quantum theory of atoms in molecules, electron density $_\rho$(r) is the more precise description of the electronic structure of the molecules. It is crucial to concentrate on non-covalent interactions since they play a significant role in molecular packing. The determination of electron density $_\rho$(r) and its Laplacian ∇^2_ρ(r) helps to find out whether H-bond is present between acceptor and donor group. The electron density and magnitude of the Laplacian at the bond critical point (BCP) represent the strength and kind of the interactions existing in the molecule respectively. The topological parameters are determined at BCP (3, -1) for intramolecular H-bonds. The analysis of intramolecular interaction in molecules by the framework of QTAIM is represented in (**Fig. 7**). The electron density value is found to be 0.29614 for the S(6) ring (H16-C16-C11-C10-C9-H9) formed due to the intramolecular short interaction (**Fig. 7**), respective value of ∇^2_ρ(r) is negative and the ratio of $|G(r)|/V(r)$ is greater than unity (i.e>1) confirms the non-covalent interaction. Only critical points in the electron density are used in the QTAIM analysis, leaving out some weak interactions. To conquer this problem, non-covalent interactions (NCI) is employed to evaluate intramolecular interactions based on reduced density gradient (RDG) and its first derivative $\nabla\rho$(r) (RDG is the region where the electron density is low). To identify the locations with non-covalent interactions where RDG goes to zero at low densities, one can effectively use the NCI index. The NCI iso surface depicted several sorts of interactions using a colour scale that helps to distinguish between them based on the sign of the electron density Hessian matrix ($\lambda2$), where ($\lambda2$), if $\lambda2 >0$ denotes repulsion and $\lambda2<0$ denotes attraction. Blue colours indicate strong attractive interactions (H-bond), red colour represents repulsive interaction (steric clashes), and where as green colour represents weak interactions such as van der Waals interactions.The 2D NCI scatter plots of RDG against sign $(_{\lambda2})_\rho(r)$ for the DMC molecule is shown in (**Fig. 7**), which confirms the non-covalent interactions involved in the molecule. The low density spikes lying at negative values (-0.02 to 0.01) confirms attractive noncovalent interactions. The peaks in the region (sign$(_{\lambda2})_\rho(r)$ -0.04) are indicators of stronger and more stabilizing interactions that are attributed to the molecular packing. The spikes lying at (sign$(_{\lambda2})_\rho(r)$ >0.01) are stronger repulsion or steric clashes present in the benzene rings of the DMC molecule. The prominent (C-H...O) hydrogen bond is absent in QTAIM analysis (**Fig. 7**). whereas it appears in NCI analysis shown in (**Fig. 7**).
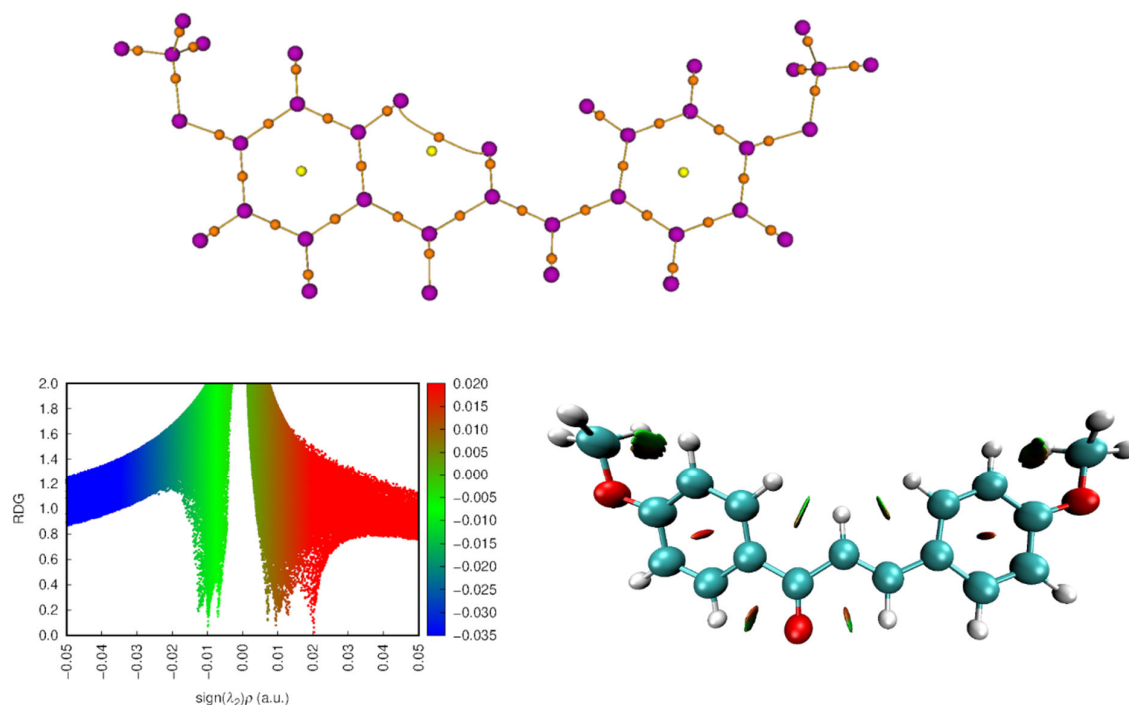

Fig. 7. QTAIM and NCI plots of intramolecular interactions.

Molecular docking studies

As we discussed in the introduction part, to assess the interactions of our DMC molecule with covid-19 main protease (6LU7), docking studies were carried out. (**Fig. 8**) show the binding mode of the molecule revealed that 4,4-Dimethoxychalconeis binded into an active site of protein with a good binding score of -6.0 kcal/mol. The detailed interaction between the ligand and protein (bond length and interaction type) is shown in (**supplementary Table S3**) DMC molecule interacted with the active site residues (GLU166, CYS145, SER144, THR25) of target protein through various interactions such as conventional H-bond, Pi-alkyl, C-H bond, and Pi-sigma. The significant interactions between DMC

molecules and 6LU7 protein are also described by π-alkyl and π-sigma interactions between centroids of the benzene rings (**Fig. 8c and supplementary Table S3**).
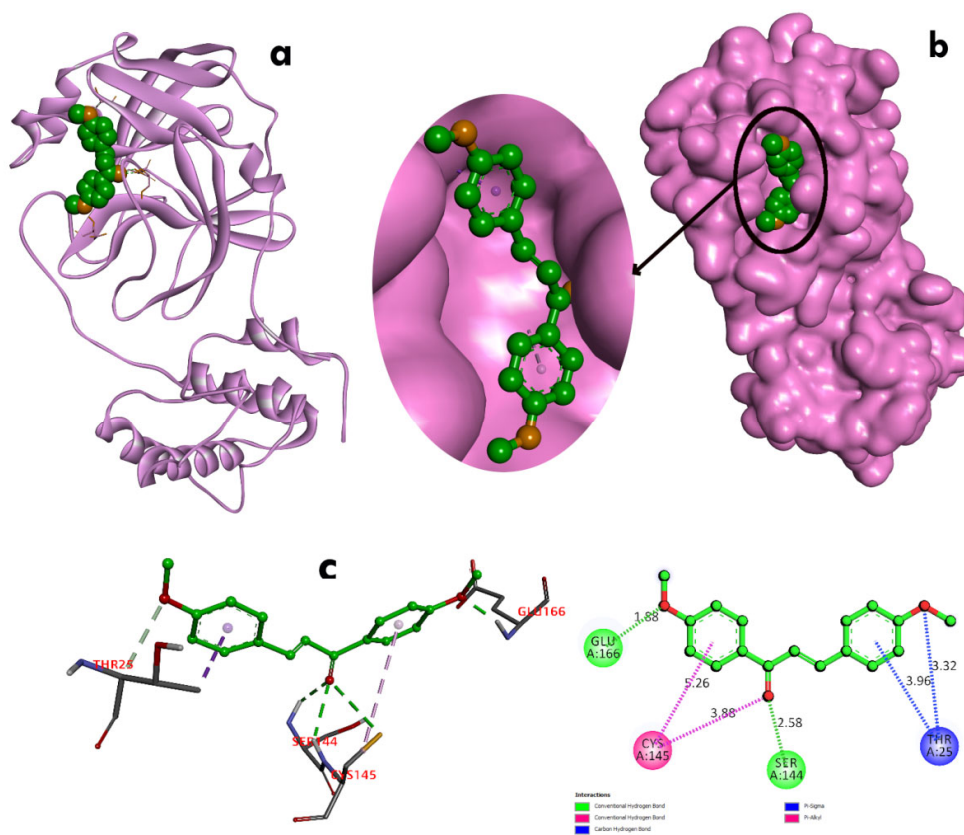

Fig. 8. DMC molecule docked with COVID-19 main protease: Cartoon representation (a), surface representation (b) and (c) 3D and 2D view of interactions between DMC molecule and main protease.

2.6 Molecular dynamic simulations

For further examination of the molecular docking studies, the molecular dynamic simulation was performed. To investigate the binding mode stability and interactions between the targeted protein and the test DMC molecule, a simulation run spanning 100ns was conducted. The protein-ligand complex was analysed by the root mean square deviation (RMSD), root mean square fluctuations (RMSF), and protein-ligand interactions to evaluate the dynamic characteristics over the simulation period.

RMSD: RMSD of the protein-ligand complex was examined during the 30ns MD simulation to measure the equilibration, protein flexibility, conformational changes, translational and rotational movements inside the protein binding site. (**Fig. 9a and Fig. 9d**) depicts the RMSD plot and the corresponding selected trajectory (1, 10, 20 and 30ns) images for ligand-protein complex. DMC molecule showed a good stability, as this molecule is equilibrated at 0ns, vibrated about up to ~10ns and then stable in between span of ~2.0 Å during the entire simulation period. 6LU7 protein RMSD showed small variations and subsequently stabilized in the range between ~1.2 to 2.5 Å. The oscillations in the RMSD values for the DMC-6LU7 complex indicate the durability of hydrogen and other bond interactions and showed the molecule is more active inside the binding pocket of protein.

RMSF: RMSF for protein-ligand complex was measured based on the fluctuations at the residue level. To explore more insight of the protein flexibility, the time average of RMSF values of the all amino acids of 6LU7 protein with the presence of DMC molecule were calculated over the simulation period. The RMSF plot indicated that binding to the receptor was stable and showed minor effect on the flexibility of the protein throughout the simulation period (**Fig. 9b**). The maximum fluctuation in the RMSF plot was observed for the residues ASN277 (2.02 Å), GLN273 (1.67 Å), GLN244 (1.36 Å) and ASN142 (1.1.56 Å). The active site residues CYS145 (0.52 Å), SER144 (0.61 Å), GLU166 (0.75 Å) and THR25 (0.88 Å) which are contributed in the protein-ligand binding showed very less fluctuations. In the RMSF plot, residues which interact with the ligand are spotted with green-colored vertical bars. THR24 (1.14 Å), THR25 (0.88 Å), THR26 (0.79 Å), HIS41

(1.15 Å), LEU50 (0.1.07 Å), VAL42 (0.70 Å), ASN119 (1.07 Å), CYS145 (0.52 Å), HIS164 (0.51 Å), GLU166 (0.75 Å), LEU167 (0.84 Å), ALA173 (0.59 Å) and ASP187 (0.92Å) are the few residues interacted during simulation period and showed less fluctuations.

Protein-ligand interactions: Owing to their strong impact on drug specificity, metabolization and adsorption, hydrogen bonds are very important in drug design. It is clear from the fingerprint image of the DMC interaction at the protein active site, the residues GLU166, and GLN189 maintained their hydrogen bonds with the ligand during the simulation period (**Fig. 9c**). These residues formed hydrogen-bonded interactions with the DMC molecule, mediated by water molecules. PRO168, LEU50 and CYS45 residues sustained their hydrophobic interactions (π-cation and π-π) with the aromatic groups of DMC which also significantly contribute to the overall protein-ligand stability during the simulation period. This work confirms the importance of organic compounds and other applied fields in nature.
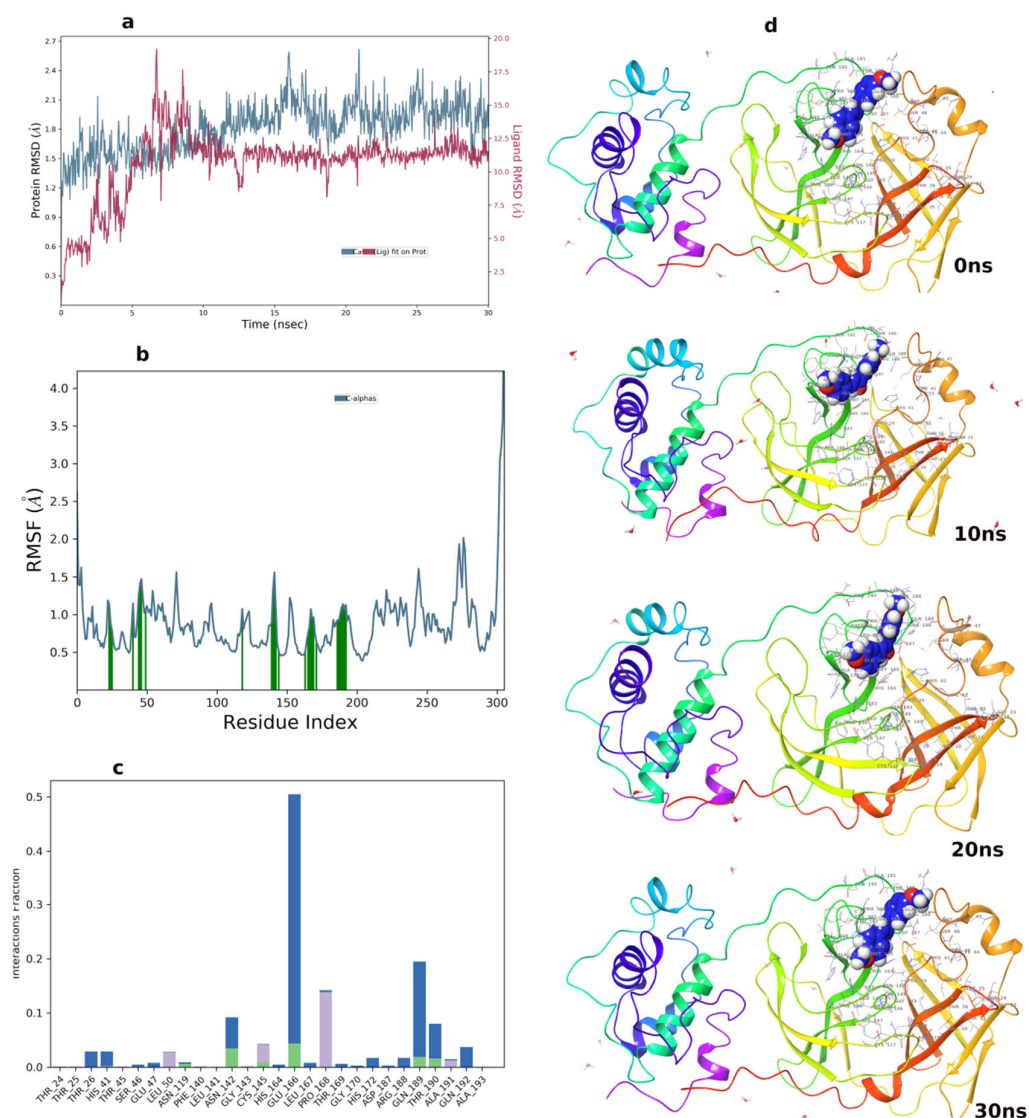

Fig. 9. RMSD profile of protein-ligand complex and RMSF profile of 6LU7 protein residues.

3. Conclusion

The title compound 4,4-Dimethoxychalcone was re-crystallized and the structure was confirmed by X-ray diffraction technique. Structural analysis reveals that the crystal packing exhibits both intra and intermolecular hydrogen bond interactions which are responsible for the formation of supramolecular synthons. Intermolecular interactions are quantified by Hirshfeld surface analysis, where H…H interactions (42%) significantly contribute to the total Hirshfeld surface. Molecular docking of title compound with M^{pro} of COVID-19 (PDB ID:6LU7) is performed and the binding affinity of -6.0 kcal/mol is obtained and the interactions between the ligand and the amino acid residues of the receptor are investigated

by molecular dynamics (MD) for 30 ns. The current study's findings indicate that DMC was expected to be a substantial inhibitor of SARS-CoV-2. Further, its potential has to be assessed by *in-vitro, in-vivo* and clinical studies.

4. Experimental

4.1 Materials and method

4,4-Dimethoxychalcone (DMC) compound was purchased from the Sigma Aldridge chemicals. DMC was re-crystallized using slow evaporation method referring Ravindra *et al.,* [25]. A good quality single was chosen for X-ray diffraction data collection. X-ray intensity data were collected at 293K using graphite-monochromated Mo-Kα(λ=0.71073Å) radiation which is equipped with RigakuX-taLAB mini three-circle CCD diffractometer. The data collection and reduction were carried out using the CrystalClear-SM Expert 2 and d*TREK program using SHELXS and SHELXL [26-27]. Structure solution was obtained by direct methods and the coordinates were refined by full matrix least-squares against F^2. Crystal structure geometry calculations were carried out using PLATON [28], and the molecular graphics were generated using MERCURY 4.2.0 [29].

Hirshfeld surface and Energy framework analysis

Hirshfeld surface (HS) analysis is a unique approach to describe the surface characteristic of molecule and to visualize the intermolecular interactions exhibited by the molecule in a crystalline environment. To verify the various types of non-covalent interactions existing in the crystal structure, molecular Hirshfeld surfaces plots and their 2D fingerprint plots (FP2) were generated using CrystalExplorer 3.1 [30] software on the basis of a crystallographic information file (CIF). Energy frame work offer a powerful and unique way to visualize the supramolecular architecture of molecular crystal structures. The cylinders that make up the framework represent the relative strengths of molecular packing in different direction and with different magnitude [31,32]. The energy framework calculations were carried out using B3LYP/6-31G (d, p) functional basis set. A cluster of molecules within a radius of 3.8 Å and 20 Å were generated around a single molecule for interaction energy and lattice energy respectively. The interaction energies (electrostatic, polarization, dispersion, and repulsion) between the molecular pairs and the lattice energy of the molecule were calculated using *Crystal Explorer* [30].

Density functional theory calculation

Density functional theory (DFT) is used to computing electronic wave functions of DMC. The prominent approximation to the wave functions is its lowest energy state and this can be attained by optimizing the molecular coordinates to its ground state level. The most stable calculated conformation is the basis for further theoretical calculations. DMC molecular structure is optimized in gas phase using DFT with B3LYP hybrid functional at 6-311G+(d, p) level basis set. The KohnSham molecular orbitals, their energy gap the related global and local indexes were explored with Koopman's approximation. The molecular electrostatic potential (MEP) map shows electronegative and electropositive active sites of the molecule. All these calculations were executed using *Gaussian 16* package and were visualized using *GaussView* [33, 34].

Molecular docking studies

To investigate the effect of DMC molecule with the COVID-19 main protease, molecular docking analysis was carried out. MGL tools 1.5.6 [35] with AutoDock Vina [36, 37] were used for the molecular docking analysis to detect the preferred binding sites. Crystallographic information files of DMC was used for the ligand preparation and the structure was optimized and energy minimized by MGL tools 1.5.6. From the Protein Data Bank, three-dimensional structure of main protease (PDB ID:6LU7) was downloaded in PDB format. The initial preparation of the protein structure was performed by removing water and N3 inhibitor using Biovia Discovery Studio 2019 visualizer [38-43]. Then using AutoDock Tools nonpolar hydrogen atoms were added and energy minimized to the main protease. The atomic potential binding site was defined using grid size of x = -11.575, y = 14.611 and z = 65.164. The binding affinity of the DMC was observed as a negative score with the unit of kcal/mole. The ligand interactions were visualized and analysed using Biovia Discovery Studio 2019 visualizer.

Molecular dynamic (MD) simulation studies

The MD simulation of a DMC-6LU7 protein complex was carried out using the academic version of the Desmond modules in the Schrodinger 2020–2 suite. A better docking result was chosen for the molecular dynamics (MD) simulation to determine the DMC stability with the targeted protein. The cubic box was inundated with TIP3P water molecules with a simple point charge. The system was solvated, and the OPLS3 force field was used to prepare and evaluate the complex. To keep the system neutral, the minimum quantity of Na^+ ions and salt atoms were added. The compound was introduced

using a conjugated algorithm with a 1 kcal/mol convergence threshold. The relaxed system was then subjected to 30ns MD simulations with a Marlyna-Tobias-Klein barostat set to 1 bar pressure and a Nose-Hoover thermostat set to 300 K under NPT ensemble. The energy potential stability of the protein-ligand complex system and protein-ligand interaction were investigated using a root mean square deviation (RMSD) and root mean square fluctuations (RMSF).

4.2 Supplementary crystallographic data

CCDC 2208035 contain the supplementary crystallographic data for this compound, and can be obtained free of charge from the Cambridge Crystallographic Data Centre via www.ccdc.cam.ac.uk/data_request/cif.

References

1. Sarda, S. R., Puri, V. A., Rode, A. B., Dalawe, T. N., Jadhav, W. N., & Pawar, R. P. (**2007**). Sulfated tin oxides: a suitable reagent for synthesis of 2, 4-diphenyl-4, 6, 7, 8-tetrahydrochromen-5-one. Arkivoc, 16, 246-251.

2. Hemingway, R. W. (**1989**). Structural variations in proanthocyanidins and their derivatives. In *Chem and significance of condensed tannins* (pp. 83-107). Springer, Boston, MA.

3. Harborne, J. B., Mabry, T. J. and Mabry, H. (**1975**). The Flavonoids Chapman and Hall. Biochemical systematics of flavonoids.

4. Pawlak, A., Henklewska, M., Hernández Suárez, B., Łużny, M., Kozłowska, E., Obmińska-Mrukowicz, B., & Janeczko, T. (**2020**). Chalcone methoxy derivatives exhibit antiproliferative and proapoptotic activity on canine lymphoma and leukemia cells. *Molecules*, *25*(19), 4362.

5. Opletalova, V. (**2000**). Chalcones and their heterocyclic analogs as potential therapeutic agents in bacterial diseases. *Ceska a Slovenska Farmacie: Casopis Ceske Farmaceuticke Spolecnosti a Slovenske Farmaceuticke Spolecnosti, 49*(6), 278-284.

6. Konieczny, M. T., Konieczny, W., Sabisz, M., Skladanowski, A.,Wakiec, R., ´ Augustynowicz-Kopec, E. and Zwolska, Z. (**2007**). Synthesis of isomeric, oxathiolone fused chalcones, and comparisonof their activity toward various microorganisms and human cancercells line. *Chem. Pharm. Bull., 55*(5), 817-820.

7. Narender, T., Khaliq, T., Goyal, N., & Gupta, S. (**2005**). Synthesis of chromenochalcones and evaluation of their in vitro antileishmanial activity. *Bioorg. Med. Chem.,* 13(23), 6543-6550.

8. Lee, S. H., Nan, J. X., Zhao, Y. Z., Woo, S. W., Park, E. J., Kang, T. H., ... & Sohn, D. H. (**2003**). The chalcone butein from Rhus verniciflua shows antifibrogenic activity. *Planta Med., 69*(11), 990-994.

9. Jin, F., Jin, X. Y., Jin, Y. L., Sohn, D. W., Kim, S. A., Sohn, D. H., ... & Kim, H. S. (**2007**). Structural requirements of 2′, 4′, 6′-tris (methoxymethoxy) chalcone derivatives for anti-inflammatory activity: The importance of a 2′-hydroxy moiety. *Archives of pharmacal research, 30*(11), 1359-1367.

10. Barfod, L., Kemp, K., Hansen, M., & Kharazmi, A. (**2002**). Chalcones from Chinese liquorice inhibit proliferation of T cells and production of cytokines. *Int. Immunopharmacol., 2*(4), 545-555.

11. Prasad, Y. R., Rao, A. L., & Rambabu, R. (**2008**). Synthesis and antimicrobial activity of some chalcone derivatives. *J Chem, 5*(3), 461-466.

12. Havranek, B., & Islam, S. M. (**2021**). An in silico approach for identification of novel inhibitors as potential therapeutics targeting COVID-19 main protease. *Journal of Biomolecular Structure and Dynamics, 39*(12), 4304-4315.

13. Bheenaveni, R. S. (**2020**). India's indigenous idea of herd immunity: the solution for COVID-19?. *Tradit. Med. Res., 5*(4), 182.

14. Clarke, J. M., Majeed, A., & Beaney, T. (**2021**). Measuring the impact of covid-19. bmj, 373.

15. Fehr, A. R., & Perlman, S. (**2015**). Coronaviruses: an overview of their replication and pathogenesis. *Coronaviruses*, 1-23.

16. Ziebuhr, J., & Siddell, S. G. (**1999**). Processing of the human coronavirus 229E replicase polyproteins by the virus-encoded 3C-like proteinase: identification of proteolytic products and cleavage sites common to pp1a and pp1ab. *Virol. J., 73*(1), 177-185.

17. Thiel, V., Ivanov, K. A., Putics, A., Hertzig, T., Schelle, B., Bayer, S., & Ziebuhr, J. (**2003**). Mechanisms and enzymes involved in SARS coronavirus genome expression. *J. Gen. Virol., 84*(9), 2305-2315.

18. Snijder, E. J., Bredenbeek, P. J., Dobbe, J. C., Thiel, V., Ziebuhr, J., Poon, L. L., ... & Gorbalenya, A. E. (**2003**). Unique and conserved features of genome and proteome of SARS-coronavirus, an early split-off from the coronavirus group 2 lineage. *J. Mol. Biol., 331*(5), 991-1004.

19. Ziebuhr, J., Heusipp, G., & Siddell, S. G. (**1997**). Biosynthesis, purification, and characterization of the human coronavirus 229E 3C-like proteinase. *Virol. J., 71*(5), 3992-3997.

20. Hatada, R., Okuwaki, K., Mochizuki, Y., Handa, Y., Fukuzawa, K., Komeiji, Y., ... & Tanaka, S. (**2020**). Fragment molecular orbital based interaction analyses on COVID-19 main protease− inhibitor N3 complex (PDB ID: 6LU7). *J Chem Inf Model, 60*(7), 3593-3602.

21. Zhang, L., Lin, D., Sun, X., Curth, U., Drosten, C., Sauerhering, L., ... & Hilgenfeld, R. (**2020**). Crystal structure of SARS-CoV-2 main protease provides a basis for design of improved α-ketoamide inhibitors. *Science, 368*(6489), 409-412.

22. Yang, S., Chen, S. J., Hsu, M. F., Wu, J. D., Tseng, C. T. K., Liu, Y. F., ... & Hsu, M. C. (**2006**). Synthesis, crystal structure, structure– activity relationships, and antiviral activity of a potent SARS coronavirus 3CL protease inhibitor. *J. Med. Chem., 49*(16), 4971-4980.

23. Chen, S., Hu, T., Zhang, J., Chen, J., Chen, K., Ding, J., ... & Shen, X. (**2008**). Mutation of Gly-11 on the dimer interface results in the complete crystallographic dimer dissociation of severe acute respiratory syndrome coronavirus 3C-like protease: crystal structure with molecular dynamics simulations. *J. Biol. Chem., 283*(1), 554-564.

24. Ravindra, H. J., Harrison, W. T. A., Kumar, M. S., & Dharmaprakash, S. M. (**2009**). Synthesis, crystal growth, characterization and structure–NLO property relationship in 1, 3-bis (4-methoxyphenyl) prop-2-en-1-one single crystal. *Journal of crystal growth, 311*(2), 310-315.

25. Expert, C. S. (2011). Rigaku Corporation. Tokyo, Japan.

26. Sheldrick, G. M. (**2008**). A short history of SHELX. *Acta Crystallogr. A ACTA CRYSTALLOGR A, 64*(1), 112-122.

27. Minor, W., Dauter, Z., Helliwell, J. R., Jaskolski, M., & Wlodawer, A. (**2016**). Safeguarding structural data repositories against bad apples. *Structure, 24*(2), 216-220.

28. Hema, M. K., Karthik, C. S., Pampa, K. J., Manukumar, H. M., Mallu, P., Warad, I., & Lokanath, N. K. (**2019**). Solvent induced 4, 4, 4-trifluoro-1-(2-naphthyl)-1, 3-butanedione Cu (II) complexes: Synthesis, structure, DFT calculation and biocidal activity. *Polyhedron, 168*, 127-137.

29. Spackman, P. R., Turner, M. J., McKinnon, J. J., Wolff, S. K., Grimwood, D. J., Jayatilaka, D., & Spackman, M. A. (**2021**). CrystalExplorer: A program for Hirshfeld surface analysis, visualization and quantitative analysis of molecular crystals. *J. Appl. Crystallogr., 54*(3), 1006-1011.

30. Pampa, K. J., Karthik, C. S., Hema, M. K., Mallu, P., & Lokanath, N. K. (**2021**). Post-synthetic modification of supramolecular assemblies of β-diketonato Cu (II) complexes: comparing and contrasting the molecular topology by crystal structure and quantum computational studies. *Cryst. Eng. Comm., 23*(24), 4344-4369.

31. Hema, M. K., Karthik, C. S., Pampa, K. J., Mallu, P., & Lokanath, N. K. (**2020**). Solvent induced mononuclear and dinuclear mixed ligand Cu (II) complex: structural diversity, supramolecular packing polymorphism and molecular docking studies. *New J. Chem., 44*(41), 18048-18068.

32. Frisch, M. E., Trucks, G. W., Schlegel, H. B., Scuseria, G. E., Robb, M. A., Cheeseman, J. R., ... & Fox, D. J. (**2016**). Gaussian 16.

33. Dewar, M. J., Holder, A. J., Dennington, R. D., Liotard, I. D. A., Truhlar, D. G., Keith, T. A., ... & Harris, C. D. (**1994**). AMPAC 8 User Manual.

34. Agrahari, A. K. (**2017**). A computational approach to identify a potential alternative drug with its positive impact toward PMP22. *J. Cell. Biochem., 118*(11), 3730-3743.

35. Trott, O., & Olson, A. J. (**2010**). AutoDock Vina: improving the speed and accuracy of docking with a new scoring function, efficient optimization, and multithreading. *J. Comput. Chem., 31*(2), 455-461.

36. Huey, R., Morris, G. M., & Forli, S. (**2012**). Using AutoDock 4 and AutoDock vina with AutoDockTools: a tutorial. *The Scripps Research Institute Molecular Graphics Laboratory*, 10550, 92037.

37. Studio, D. (**2008**). Discovery studio. *Accelrys* [2.1].

38. Mohamed, S. K., Mague, J. T., Akkurt, M., Alfayomy, A. M., Seri, S. M. A., Abdel-Raheem, S. A., & Ul-Malik, M. A. A. (**2022**). Crystal structure and Hirshfeld surface analysis of ethyl (3E)-5-(4-chlorophenyl)-3-{[(4-chlorophenyl) formamido] imino}-7-methyl-2H, 3H, 5H-[1, 3] thiazolo [3, 2-a] pyrimidine-6-carboxylate. *Acta Crystallogr. E: Crystallogr. Commun., 78*(8).

39. Kaid, M., Ali, A., Shamsan, A., Younes, S., Abdel-Raheem, S., Abdul-Malik, M & Salem, W. (**2022**). Efficiency of maturation oxidation ponds as a post-treatment technique of wastewater. *Curr. Chem. Lett., 11*(4), 415-422.

40. Fouad, M., Badawy, M., El-Aswad, A., & Aly, M. (**2023**). Experimental modeling design to study the effect of different soil treatments on the dissipation of metribuzin herbicide with effect on dehydrogenase activity. *Curr. Chem. Lett., 12*(2), 383-396.

41. Tolba, M., ul-Malik, M., El-Dean, A., Geies, A., Radwan, S., Zaki, R., Sayed, M., Mohamed, S & Abdel-Raheem, S. (**2022**). An overview on synthesis and reactions of coumarin based compounds. *Curr. Chem. Lett., 11*(1), 29-42.

42. Abd-Ella, A., Metwally, S., ul-Malik, M., El-Ossaily, Y., Elrazek, F., Aref, S., Naffea, Y & Abdel-Raheem, S. (**2022**). A review on recent advances for the synthesis of bioactive pyrazolinone and pyrazolidinedione derivatives. *Curr. Chem. Lett., 11*(2), 157-172.

43. Abdel-Raheem, S., El-Dean, A., Hassanien, R., El-Sayed, M., Abd-Ella, A., Zawam, S., & Tolba, M. (**2022**). Synthesis of new distyrylpyridine analogues bearing amide substructure as effective insecticidal agents. *Curr. Chem. Lett., 11*(1), 23-28.